Applied Energy 229 (2018) 828–840

Contents lists available at ScienceDirect

Applied Energy

journal homepage: www.elsevier.com/locate/apenergy

Oxy-fuel combustion in a two-pass oxygen transport reactor for fire tube boiler application

Ibrahim B. Mansir*, Rached Ben-Mansour, Mohamed A. Habib

KACST TIC on CCS and Mechanical Engineering Department, King Fahd University of Petroleum & Minerals, Dhahran 31261, Saudi Arabia

HIGHLIGHTS

- Simulation of two-pass oxygen transport membrane (OTM) reactor for fire tube boiler.
- Gas inlet conditions dictate the rate of oxygen permeation under reactive conditions.
- Gas inlet temperature and mass flowrates control the amount of heat transfer to load.
- Sweep gas inlet condition was more critical to the stability of combustion reaction.
- The proposed design of the OTM reactor can deliver power range of 1–5 MWe.

ARTICLE INFO

Keywords:
Carbon capture
Oxy-fuel combustion
Oxygen transport membrane
Fire-tube boiler

ABSTRACT

Application of oxy-fuel combustion carbon capture technology to power plants is currently getting special attention as one of the means of curtailing CO_2 emission responsible for the current climate change. The key concept of oxy-fuel combustion technology is the use of pure oxygen, obtained via air separation technologies, for combustion instead of air. Currently, the membrane separation technology is gaining high momentum due to its flexibility for different applications. Integrating oxygen transport membrane reactors to fire tube boilers has the prospects of concurrent permeation of oxygen, in-situ combustion as well as steam generation within a confined space, thus, potential for more compact boilers. Despite the in-situ prospects of the Oxygen Transport Membrane (OTM) integration, it comes with the heat transfer design challenges due to fragile nature of the membrane as well as maintaining the required operating temperatures for optimum performance. Hence the geometry as well as the heat transfer characteristics need to be well designed and the system needs to be thoroughly investigated for optimum performance. In this study, numerical modeling of a two-pass oxygen transport membrane reactor for oxygen permeation and oxy-fuel combustion characteristics analyses for fire tube boilers application was conducted. It was found that, for the non-reactive conditions, the effects of gases inlet temperature and mass flow rates on oxygen permeation along the length of the membrane was meager within the scope of this study. The gases inlet conditions dictate the rate of oxygen permeation under reactive conditions. Also, the gases inlet temperature and mass flow rates control the amount of heat transfer to the load. The sweep gas inlet condition was more critical to the stability of the combustion reaction. The current design of the proposed OTM reactor can deliver power output in the range from 1 to 5 MWe when applied to a typical fire-tube boiler.

1. Introduction

The largest source of carbon dioxide (CO_2) emission into the atmosphere is believed to come from the combustion of fossil-based fuels in power plants. The CO_2 emission is considered as the major greenhouse gas responsible for the current global climate change. As reported by the International Energy Agency, the global energy consumption based on fossil fuel amounts to about 80% of the total global energy demand. This results in the emission of 32.3 Gt of CO_2 to the atmosphere in the year 2014 [1]. Recent findings indicated that about 40% of the global CO_2 emission is a result of electricity generation, with more than 30% coming from fossil fuels [1]. The current and future energy policy will be shaped by the fight against climate change, by committing to the emission reductions pledged by countries under the

* Corresponding author.
E-mail address: ibrahimmb@kfupm.edu.sa (I.B. Mansir).

https://doi.org/10.1016/j.apenergy.2018.08.057
Received 27 April 2018; Received in revised form 9 August 2018; Accepted 12 August 2018
Available online 17 August 2018

Nomenclature

Symbols

C_p	specific heat
$D_{i,j}$	binary mass diffusion coefficient
$D_{i,m}$	diffusion coefficient of the ith specie
D_v	bulk diffusion coefficient
I	radiation intensity
Jo_2	oxygen permeation flux
K_f	forward reaction rate constant
K_r	reverse reaction rate constant
$\dot{m}_{exh}$	exhaust mass flowrate
$\dot{m}_{feed}$	feed inlet mass flowrate
$\dot{m}o_2$	oxygen mass flowrate
Mo_2	oxygen molecular weight
$P_{O2\text{-}f}$	oxygen partial pressure at feed side
$P_{O2\text{-}s}$	oxygen partial pressure at sweep side
r	position
R_i	rate of production of *i*-th specie
s	path length
S_h	energy source term
S_i	mass source term
T_{feed}	feed inlet temperature
T_{sat}	saturation temperature
T_{sweep}	sweep inlet temperature
κ	absorption coefficient
ρ	density
σ_s	scattering coefficient
∇	divergence operator

Abbreviations

A	area
AMG	advanced Multi-Grid
BSCF	$Ba_{0.5}Sr_{0.5}Co_{0.8}Fe_{0.2}O_{3\delta}$
CCS	carbon capture and sequestration
DO	discrete ordinate
GHG	green house gases
ITM	ion transport membrane
OTM	oxygen transport membrane
OTR	oxygen transport reactor
P	pressure
RTE	radiative transfer equation
T	temperature
TIC	technology innovation center
UDF	user defined function
v	velocity
V	volume
WD	westbrook and dryer

United Nations Framework Convention on Climate Change (UNFCCC) to achieve the below 2 °C temperature rise by 2050 as agreed in Paris, 2015. In order to achieve the targeted 2 °C temperature rise limit by 2050, one-sixth of the planned reduction in GHG emissions, is anticipated to be achieved through the application of CCS technologies [2]. There exist several technologies aiming at reducing the emission of greenhouse gas by capturing the CO_2 in the utility industries. These include pre-, post- and oxy-fuel combustion carbon capture technologies. Oxy-fuel combustion technology has the potential of zero emission due to the use of oxygen only instead of air in which near stoichiometry, the end products of the combustion are mainly CO_2 and H_2O. The water vapor can easily be condensed, and the CO_2 stored. But the oxy-fuel combustion process is associated with high temperatures and hence recirculating the flue gas (mainly CO_2) or other inert gas lowers the combustion temperatures [3,4]. Application of oxy-fuel combustion technology to power plants is currently getting special attention. In a review conducted by Yin and Yan [5], it was asserted that research and development in oxyfuel combustion of pulverized fuel has been recently gaining momentum as a promising power plant technology for carbon capture. It was reported that the technical challenges posed by the influence of CO_2 as diluent during oxyfuel combustion needs to be addressed. The work focused on the implementation of the combustion physics and chemistry into CFD modeling of oxyfuel combustion. As reported by Buhre et al. [6], there was one-third reduction in NOx emissions and decrease in CO from a conventional coal-fired boiler as the result of integrating oxy-fuel combustion technology. Replacing N_2 from air with CO_2 as diluent in oxy-fuel combustion resulted in lesser fuel consumption as well as lower combustion temperatures [7,8]. The characteristics of flue gas recirculation for oxy-coal combustion was conducted by Hu and Yan [9]. They found that increase the oxidant O_2 resulted in the decrease in flue gas recirculation. The effect of exhaust gas recirculation on oxy-coal power generation system was conducted by Hu et al. [10] to assess the configuration options for emission removals in oxy-coal combustion systems by conducting performance analyses. It was reported that the recirculation options have clear effect of the radiative properties of the flue gas due to compositional change. The cost of the conventional cryogenic air separation process as well as its thermodynamic inefficiency has been the driving force for the quest of Ion Transport Membranes (ITM) as alternatives [11]. They are mostly dense, mixed conducting and nonporous ceramics materials that permit electrons and oxygen ions transport from the higher to the lower oxygen partial pressure sides at higher temperatures [12]. The factors influencing the permeation flux of oxygen depends on the type of materials and thickness of membrane along with the conditions of the oxygen permeation such as temperature and pressure, as well as sweep gas flow rate [13]. Axisymmetric geometry has been the most widely adopted design for the ITM reactors [14].

There are several literatures investigating the oxygen permeation performance across perovskite membranes. The prominent ones that studied the permeation performance at higher pressures were reported by [15–17]. The oxygen permeation flux was found to increase linearly with increase in the logarithmic value of p'_{O2}/p''_{O2}, where p'_{O2} and p''_{O2} are the feed and permeate sides oxygen partial pressures, respectively. Therefore, high oxygen permeation flux can be achieved by supplying high pressure air. The effect of membrane thickness on oxygen permeation flux on has been observed by many researchers [18–22]. They concluded that increase in membrane thickness reduces the oxygen permeation flux due to the effect of bulk diffusion. The critical membrane thickness was obtained to be approximately 1.0 mm for the membrane operating temperature range of 700–1000 °C [19]. Temperature has been among the most sensitive factors influencing oxygen permeation flux of membranes. Among the countless literatures that reported increase in O_2 permeation due to temperature increase include [18,23–26]. The oxygen permeation flux was insignificant at temperatures below 600 °C. While, when the temperature was increased to 650 °C, there were significant oxygen permeation flux with sharp increase when the temperature was above 800 °C as the result of improved surface reaction rate and/or oxygen ionic diffusion.

The effect of CO_2 as a diluent on oxy-methane combustion for lowering flame speed and adiabatic flame temperature leading to a more stable operation was reported by Khalil and Gupta [27]. They obtained a stable flame by decreasing the oxygen concentration to less than 27% and the flame blown off when further reduced the oxygen concentration to about 21%. The prospects of improving plant efficiency by over 4% by utilizing a state-of-the-art perovskite BSCF membrane as compared to the use of existing cryogenic technology has

been echoed by Castillo [28]. Fairly recently, Mezghani and Hamza [29] reported that Ba0.5Sr0.5Co0.8Fe0.2O3-δ is the most promising material for ion transport membranes due to its higher oxygen permeation flux. However, the main problem associated with the use of BSCF was inadequate chemical stability in the vicinity of higher CO_2 concentrations. They use methane gas to evaluate the performance of BSCF membranes for oxy-fuel combustion applications at optimized methane flow rates of 0.65 ml/min at 920 °C. They reported that the BSCF membrane was more stable when operating at fuel lean mixture. The rate of oxygen permeation of the membrane reduces when all the oxygen generated is instantly consumed during the combustion reaction without excess oxygen. The more the excess oxygen in the combustor the higher the long-time stability of the BSCF membrane. The performance investigation of Ba0.5Sr0.5Co0.8Fe0.2O3δ oxygen transport membrane was conducted numerically in a botton-cell reactor model for oxygen separation from air and instantaneous combustion with methane by Ahmed et al. [24]. They considered both reactive and non-reactive cases for the study of O_2 permeation and the effect of percentage of methane on reactivity. The reactivity as well as oxygen permeation were proportional to the percentage of CH_4 due to increase in volumetric flow rates. Similar findings were reported by Nemitallah [30] using oxygen permeation model for reacting flows in a modified design of the button-cell reactor to study oxy-methane combustion characteristics. An initial performance analysis of single pass carbon-free fire-tube boiler integrated with ITM has been conducted by [25] at elevated temperatures. They studied the effects of the reactor wall temperature on oxygen permeation, reaction rate as well as heat flux. Their findings indicated optimum improvement of both combustion characteristics and heat transfer at temperature of 1100 °C and 6% methane mass fraction, while the variation in fuel flow rates did not show substantial effect on the performance of the reactor due to low flow rates. In order to obtain sufficiently higher heat fluxes, they recommended scaling-up of the ITM reactor. A four-channels two-crossing membranes ITM rector geometry was utilized in the design of an ITM reactor for possible fire tube boiler applications at elevated pressure [17]. They considered a reactor length of 1.8 m and 20 bar operating pressure to determine the effects of percentage of CH_4 in the sweep side and the flow configurations on the boiler performance in the power range of 5–8 MWe. About 12,500 units of ITM reactors, 5 m high, with total volume of 45.5 m^3 was calculated. When using ITM reactors under reactive conditions with CO_2 as the diluent, the flame thickness is maximum near the surface of the membrane and the diffusion flame temperature decreases due to the influx of the cold oxygen [31]. The focus of most of the application of ITM reactors is more on to the gas turbine combustors with only few available researches on to fire tube boilers despite its eminent potentials of curving CO_2 emissions in large scale industrial boilers [32]. Hu et al. [33] investigated the effects of boiler operating conditions on the oxy-coal design and retrofitting a utility boiler. They numerically obtained comparable flame temperatures and heat transfer to the side walls of the boiler at effective oxygen concentration of about 33% by volume between the oxy-coal and air-coal combustion process.

Integrating oxygen transport membrane reactors to fire tube boilers has the prospects of concurrent permeation of oxygen, in-situ combustion as well as steam generation within a confined space, thus, potential for more compact boilers. The in-situ oxy-fuel combustion potential of this design will ensure low NOx emission and ease the carbon capture process there by making fire-tube boilers environmentally more friendly due to low GHG emission. Despite the in-situ prospects of the OTM integration, it comes with the heat transfer design challenges due to fragile nature of the membrane as well as maintaining the required operating temperatures for optimum performance. Hence the geometry as well as the heat transfer properties of a two-pass Oxygen Transport Reactor (OTR) will be designed and the system will be thoroughly investigated for optimum performance. The key controlling parameters will be parametrically studied in order to obtain optimum operating conditions. These include the effect of inlet gases temperatures and flow rates on the heat transfer to the saturated water and steam in a fire-tube boiler using methane gas. This will give more inside to the implementation of the oxy-combustion technology to fire-tube boilers in terms of air and fuel inlet conditions and the heat transfer characteristics to the typical saturated water and steam in the boilers employing methane as fuel. The amount of OTM required for the achievement of 1–5 MWe power will be estimated based on the heat transfer analyses within the OTR.

2. Mathematical formulations

2.1. Governing equations

The systems of governing equations for the modeling of the flow fields in both the air domain and the reaction zone (sweep gas domain) are determined by the set of governing equations formulated from the three-dimensional general equations of reacting flows [34]. Due to low

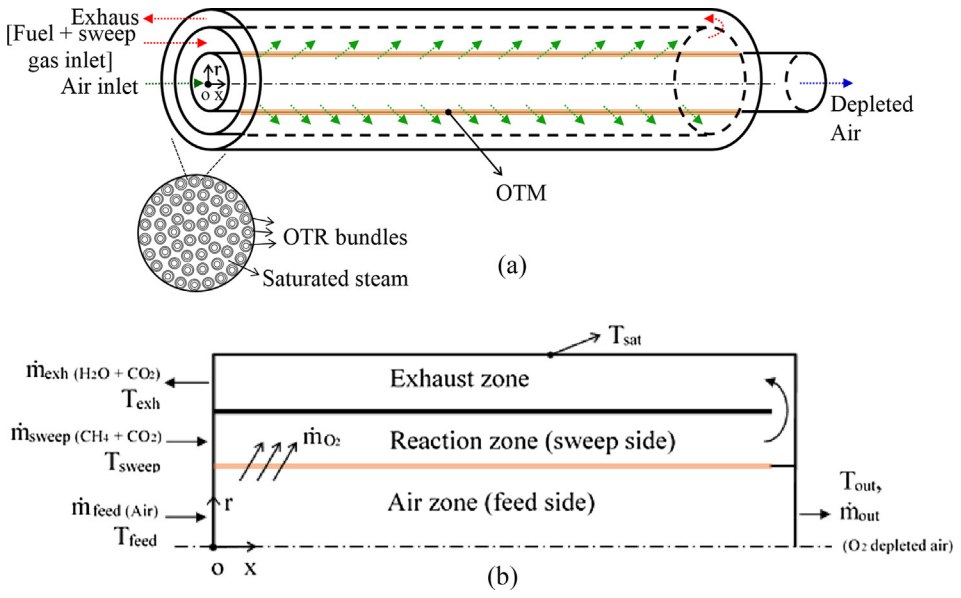

Fig. 1. (a) Schematic diagram of the OTR; (b) 2D representations of the OTR.

velocities of the inlet gases (laminar flow), only the mole fraction of oxygen that determine its partial pressure due to the dominance of thermodynamic pressure [31]. Fig. 1a shows the schematic diagram of the two-pass OTR while Fig. 1b shows the two-dimensional axisymmetric representation of the OTR with x representing the transverse axis along the OTM, y represents the axis normal to the OTM while the angular coordinate was neglected (θ-axis normal to x-r plane). The system of governing conservation equations for the numerical modeling are as follows:

$$\text{Continuity equation: } \nabla\cdot(\rho\vec{v}) = S_i \tag{1}$$

$$\text{Momentum equation: } \nabla\cdot(\rho\vec{v}\vec{v}) = -\nabla p + \mu\nabla^2\vec{v} \tag{2}$$

$$\text{Energy: } (\rho C_p)\vec{v}\cdot\nabla T = \nabla\cdot(k\nabla T) + S_h \tag{3}$$

$$\text{Species: } \nabla\cdot(\rho\vec{v}Y_i) = -\nabla\cdot(\rho D_{i,m}\nabla Y_i) + R_i + S_i \tag{4}$$

where ρ is density, $\vec{v}$ is velocity vector, S_i is mass source term, p is pressure, C_p is the specific heat of the mixture, T is temperature, k is thermal conductivity (effective), S_h is energy source term due to radiation and chemical reaction, Y_i is mass fraction of i-th specie (local), $D_{i,m}$ is diffusion coefficient of species in the mixture and R_i is the rate of production of i-th specie due to chemical reaction. The diffusion coefficient of the mixture, $D_{i,m}$ for specie transport, can be computed as (Eq. (5)) [26]:

$$D_{i,m} = \frac{1-X_i}{\sum_{j,j\neq 1}\left(\frac{X_i}{D_{i,j}}\right)} \tag{5}$$

where $D_{i,j}$ is binary mass diffusion coefficient which can be evaluated using Chapman-Enskog equation by utilizing kinetic theory [35].

In oxygen transport membrane the mass source term S_i, accounts for the oxygen mass influx into the reaction zone via permeation as well as the mass deficit (sink) of the feed zone.

$$S_i = \begin{cases} -\frac{Jo_2\cdot A_{cell}\cdot Mo_2}{V_{cell}} & feed\ side \\ +\frac{Jo_2\cdot A_{cell}\cdot Mo_2}{V_{cell}} & sweep\ zone \end{cases} \tag{6}$$

where Jo_2 is oxygen permeation flux, A_{cell} and V_{cell} are the cells' area and volume, respectively, Mo_2 is the oxygen molecular weight.

Oxy-combustion produces high temperature exhaust gases comprising of mostly CO_2 and H_2O in higher concentrations compared to the conventional air combustion reaction. Hence, In order to accurately model the thermal radiative heat transfer during oxy-fuel combustion, the non-gray gas radiation concept has to be taking into cognizance [36–38]. Hence the famous general radiative transfer equation (RTE) (Eq. (7)) will be solved using discrete ordinate (DO) approach for modeling the solid and gas mixture radiation heat transfer.

$$\text{RTE:}\frac{dI(\vec{r},\vec{s})}{ds} + (\kappa+\sigma_s)I(\vec{r},\vec{s}) = \kappa n^2\frac{\sigma T^4}{\pi} + \frac{\sigma_s}{4\pi}\int_0^{4\pi} I(\vec{r},\vec{s})\Phi(\vec{s},\vec{s}')d\Omega' \tag{7}$$

where I is radiation intensity, r and s are position and path length, respectively, κ and σ_s are absorption and scattering coefficients, respectively. The model converts the RTE into spatial coordinate system (Eq. (8)) that accounts for absorption, emission and scattering of the gas medium. The mean absorption coefficient was evaluated using the weighted sum of gray gas model [39].

$$\frac{dI(\vec{r},\vec{s})}{ds} + (\kappa+\sigma_s)I(\vec{r},\vec{s}) = \kappa I_b \tag{8}$$

2.2. OTM permeation flux

A mathematical model for predicting oxygen permeation through a BSCF membrane has recently been developed as given in Eq. (14) [21] by modifying the generalized (D_v, K_f, K_r) DKK model suggested by Xu et al., (Eq. (10)) [40]. The model incorporated the effect of the feed and sweep gas flow rates. The permeation flux is dependent on the membrane temperature (T), membrane thickness (t) and the oxygen partial pressure difference between the feed and permeate sides. The mass flow rate of oxygen permeated across the membrane is computed from Eq. (9):

$$\dot{m}_{O_2} = J_{O_2}\cdot M_{O_2}\cdot A \tag{9}$$

The general DKK model is given as:

$$J_{O_2} = \frac{D_v K_r (P^n_{O2-f} - P^n_{O2-s})}{2tK_f P^n_{O2-f}\cdot P^n_{O2-s} + D_v(P^n_{O2-f} + P^n_{O2-s})} \tag{10}$$

$$\text{where } D_v = D_v^0\cdot\exp\left(-\frac{E_D}{RT}\right) \tag{11}$$

$$K_f = k_f^0\cdot\exp\left(-\frac{E_f}{RT}\right) \tag{12}$$

$$K_r = k_r^0\cdot\exp\left(-\frac{E_r}{RT}\right) \tag{13}$$

The oxygen flux through the BSCF membrane is computed from Eqs. (14)–(17) [21]:

$$J_{O_2} = \frac{D_v K_r (P^{0.25}_{O2-f} - P^{0.25}_{O2-s})}{2tK_f P^{0.25}_{O2-f}\cdot P^{0.25}_{O2-s} + D_v(P^{0.25}_{O2-f} + P^{0.25}_{O2-s})} \tag{14}$$

$$\text{where } D_v = 5.9807\cdot 10^{-5}\cdot\exp\left(-\frac{92709}{8.314T}\right) \tag{15}$$

$$K_f = 41.688\cdot\exp\left(-\frac{146680}{8.314T}\right) \tag{16}$$

$$K_r = 1.166\cdot 10^4\cdot\exp\left(-\frac{102910}{8.314T}\right) \tag{17}$$

$P_{O2\text{-}f}$ and $P_{O2\text{-}s}$ are the oxygen partial pressures at feed and sweep side, respectively, K_r, K_f and D_v are the surface exchange reverse and forward reaction rate constants and the bulk diffusion coefficient, respectively.

2.3. Chemical reaction kinetics

A two-step reduced reaction kinetics model developed by Westbrook and Dryer mechanism consists of two reactions with the last reaction being reversible. They are expressed as follows:

$$CH_4 + 1.5O_2 \rightarrow CO + 2H_2O \tag{18}$$

$$CO + 0.5O_2 \leftrightarrow CO_2 \tag{19}$$

The mechanism consisting of two reactions of CH_4 and CO with O_2, where the reaction of CO with O_2 is a reversible reaction for CO_2 decomposition. The modified WD reaction mechanism for oxy-fuel conditions that was validated with a detailed chemical kinetic mechanism by retaining the first CH_4 and O_2 reaction, while refining the second CO-CO_2 reactions so as to improve the computation of the concentrations of major species and to account for the pressure dependence as well as the appropriate heat of reaction for the [CO]/[CO_2] equilibrium [41,42]. The modified WD reaction mechanism is shown in Table 1.

3. Solution procedure

3.1. Geometry and boundary conditions

Application of oxy-fuel combustion in a two-pass Oxygen Transport Reactor (OTR) was intended for application in fire-tube boilers, with a preliminary geometry as shown in Fig. 1. In this current design, several

Table 1
The modified Westbrook-Dryer reduced mechanism for oxyfuel reaction with kinetic rate data [J], [K], [kmol], [m] and [s] [41].

Rate of reaction [kmol/(m^{3}s)]	A	b	E
$\frac{d[CH_4]}{dt} = AT^b e^{-E/(RT)}.[CH_4]^{0.7}[O_2]^{0.8}$	5.03E11	0	2.00E08
$\frac{d[CO]}{dt} = AT^b e^{-E/(RT)}.[O_2]^{0.25}[CO][H_2O]^{0.5}$	2.24E06	0	4.18E07
$\frac{d[CO_2]}{dt} = AT^b e^{-E/(RT)}.[CO_2][O_2]^{-0.25}[H_2O]^{0.5}$	1.10E13	−0.97	3.28E08

OTR units are used in lieu of the fire tubes available in conventional fire tube boilers. The OTR will be applied to a typical fire tube boiler for the generation of power in the range from 1 to 5 MWe to be fueled by methane gas. This will involve the replacement of the fire box (burner) with bundles of tubular Oxygen Transport Membrane (OTM) combustors that will supply the required power range. The geometry consisted of concentric tubes with inner-most pipe made of OTM (1 mm thick, 20 mm internal diameter and 500 mm long). Despite the potential of increase in O_2 flux at lower OTM thickness, there is a critical thickness beyond which its structural integrity will be affected by the pressure difference across it, hence 1 mm was considered [43]. The second pipe is made of low thermal conductivity material (0.1 [W/m-K], 0.95 outer surface emissivity) with a thickness of 3 mm and outer diameter of 40 mm. The outer pipe, which is in contact with the saturated steam at constant boundary temperature (corresponding the saturation condition) is made of aluminum having internal diameter of 50 mm. Air at elevated temperature is supplied through the central pipe (feed side) while a mixture of methane and sweep gas (carbon dioxide) were supplied through the annulus between the second inner pipe and the central OTM tube. The outer annulus conveyed the exhaust gases after combustion and transferred the exhaust gas heat to the saturated steam at the outer surface of the outer pipe. Mass flow inlet boundary conditions were specified at both the sweep and feed inlet sections while pressure outlet was specified for the two exit sections. The OTM permeates oxygen ions from the feed side into the sweep side where it reacts with the CH_4 in the sweep side. The 1 mm thick BSCF membrane used has a density of 3000 kg/m^3, specific heat capacity of 0.871 kJ/kg-K and thermal conductivity of 20 W/m-K.

Due to significantly large power range of the proposed boiler as well as the current state of the art in the OTM development, the fuel, diluent as well as the air flow rates must be optimized to achieve the overall goal of carbon emission free boiler. Also, the current dependence of oxygen transport membrane on temperature elevation necessitate the temperature optimization for sufficient oxygen permeation. Hence Table 2, which shows the set of boundary conditions for the parametric studies of the effects of inlet temperature of the gases on the combustion as well as heat transfer to the saturated steam has been considered in this work. It involves three sets of boundary conditions whereby the effect feed inlet temperature cases considered were shown in the second block of Table 2, the effect of sweep gases inlet temperature cases in the third block and the combine effect of both feed and sweep temperatures shown in the last block, while keeping the mass flow rates of both the feed and sweep gases constant at 0.0005 kg/s. In a similar fashion, the effect of change in mass flow rates of the gases were considered in Table 3 while keeping the inlet temperatures of both the feed and sweep gas streams at 900 °C.

3.2. Solution procedure

Due to axisymmetric nature of the considered geometry, the oxyfuel combustion will be modelled in a single, two-dimensional OTR unit that was presented in Fig. 1. The commercial CFD code ANSYS Fluent Release: 17.1.0 was used in double precision for the combustion modelling. The solver type used for computing the solution was pressure-based, which enables the pressure-based Navier-Stokes solution algorithm. This was choosing due to the very low flow rates and its higher convergence speed. The pressure-based solver uses a coupled algorithm. This solves the pressure-based continuity equation and the momentum equations in a coupled manner. A relative velocity formulation was used since the domain was moving. Steady state, Laminar flow was considered due to the nature of the low flow rates. Energy model was used to solve the energy equations. Discrete Ordinate Model was considered for the two non-reacting species that participate in the radiation. Species transport was enabled for the mixture of the combustion exhaust gases with inlet diffusion. The set of oxygen permeation Eqs. (14)–(17) were used for the modeling the oxygen permeation flux across the tubular OTM. The generalized single finite-rate chemical kinetics model was used to simulate the chemical kinetics of the volumetric reactions. This required importing a chemical kinetic (CHEMKIN) file containing the mechanisms into the ANSYS FLUENT solver. The oxygen permeation flux equation was defined in the FLUENT 17.1.0 via a User Define Function (UDF) written in C++ language. The code was then compiled and hooked to the ANSYS FLUENT software. The possible problem of hydraulic jump across the membrane was fixed by patching the cells of the permeate as well as the sweep sides with the mass fractions of the species which determines the partial pressures of species.

The SIMPLE Pressure-Velocity coupling scheme was chosen. The discretization scheme for Pressure, Density, Momentum, Energy and Species and the Discrete Ordinate were all set to Second Order Upwind. Enhancement of the solution convergence was ensured by employing the aggressive advanced multi-grid (AMG) scheme. For the coupled equations consisting of continuity, momentum, energy, and species, AMG 'f-cycle' was set as a recursive method. To evade irregular convergence, the available bi-conjugate gradient stabilized scheme was used. The solution convergence criteria were set as below 10^{-9} for the continuity and energy residuals. Also, in order to confirm the convergence, mass fractions of carbon dioxide and water (exhaust species), outer-pipe surface heat flux and exhaust gas temperature were monitored until their values became constant. Mesh grid dependency test was performed to ensure grid independence for accurate solutions and the model was validated with available experimental data.

Table 2
Effect of feed and sweep streams inlet temperatures.

		Feed inlet temp.		Sweep inlet temp.		Feed and Sweep temp.	
$\dot{m}_{feed}$ [kg/s]	$\dot{m}_{sweep}$ [kg/s]	T_{feed} [°C]	T_{sweep} [°C]	T_{feed} [°C]	T_{sweep} [°C]	T_{feed} [°C]	T_{sweep} [°C]
5.0E−04	5.0E−04	800	900	900	800	800	800
5.0E−04	5.0E−04	850	900	900	850	850	850
5.0E−04	5.0E−04	900	900	900	900	900	900
5.0E−04	5.0E−04	950	900	900	950	950	950
5.0E−04	5.0E−04	1000	900	900	1000	1000	1000

Table 3
Effect of feed and sweep streams inlet mass flow rates.

		Feed inlet flow rate		Sweep inlet flow rate		Feed and Sweep flow rate	
T_{feed} [°C]	T_{sweep} [°C]	$\dot{m}_{feed}$ [kg/s]	$\dot{m}_{sweep}$ [kg/s]	$\dot{m}_{feed}$ [kg/s]	$\dot{m}_{sweep}$ [kg/s]	$\dot{m}_{feed}$ [kg/s]	$\dot{m}_{sweep}$ [kg/s]
900	900	1.0E−05	5.0E−04	5.0E−04	1.0E−05	1.0E−05	1.0E−05
900	900	5.0E−05	5.0E−04	5.0E−04	5.0E−05	5.0E−05	5.0E−05
900	900	1.0E−04	5.0E−04	5.0E−04	1.0E−04	1.0E−04	1.0E−04
900	900	5.0E−04	5.0E−04	5.0E−04	5.0E−04	5.0E−04	5.0E−04
900	900	1.0E−03	5.0E−04	5.0E−04	1.0E−03	1.0E−03	1.0E−03

4. Results and discussion

4.1. Mesh size independence

The mesh size independence test was performed to ensure the accuracy of the numerical solutions. The test consisted of four different discretized geometries with the number of cells ranges from 6375 to 51,000 cells (0.6375×10^4, 1.275×10^4, 2.55×10^4, 5.1×10^4 cells for mesh-1, mesh-2, mesh-3 and mesh-4, respectively). The mass flow rates of oxygen permeated across the OTM and the total heat received by the outer-pipe were computed under the same conditions using the four grid meshes and plotted in Fig. 2. The maximum variation in O_2 mass flow rate between mesh-1 and mesh-4 was found to be 2.84%, between mesh-2 and mesh-4 was 0.16%, and between mesh-3 and mesh-4 was 0.01%. Similarly, the maximum variation between the total heat received by the outer-pipe between mesh-1 and mesh-4 was found to be 0.61%, between mesh-2 and mesh-4 was 0.11%, and between mesh-3 and mesh-4 was 0.0002%. Fig. 2 elaborated these variations graphically. Both the O_2 total mass flow rates and the heat transferred were over predicted by the low-quality meshing with lower grids and the variables remains relatively constant from mesh-3 to mesh-4. From the above analysis, the variation of results of mesh-3 with respect to mesh-4 were insignificant. Hence mesh-3 was choosing for the subsequent analyses. The mesh orthogonal quality usually is in the ranges of 0–1, with values approaching 0 corresponding to low quality mesh. The maximum orthogonal skew of mesh-3 was 0 while the minimum orthogonal quality was 1 and the maximum aspect ratio was 2.23. The mesh contained 25,500 cells, having 53,086 faces and 27,583 nodes.

4.2. Model validation

The OTM permeation model presented in Eqs. (14)–(17) were applied to the experimental work conducted by Behrouzifar et al. [21,29] and Mezghani and Hamza [21,29]. In the former experiment [21,29], O_2 permeation flux was measured across a 1 cm diameter disk-shaped BSCF OTM at various values of thickness under different elevated temperature conditions without reaction under steady laminar flow. They supplied synthetic air (nitrogen + oxygen mixture) at a volume flow rate of 150 cm^3/min in the feed side and pure helium at volume flow rate of 60 cm^3/min in the permeate (sweep) side at atmospheric pressure. The experimental results at varied temperatures and membrane thickness were shown in Fig. 3, (symbols). The same conditions were modeled in this work and the comparison with the experimental data as shown in the Fig. 3 (solid lines) indicated the same trend of increase in O_2 permeation flux with increase in temperature and the inverse with increase in membrane thickness with reasonable degree of accuracy. The later experimental data of Mezghani and Hamza [21,29] was conducted using a 2.5 cm diameter disk-shaped BSCF OTM having thickness of 1 mm over a period of 100 h. They supplied helium at constant volume flow rate of 5.0E−7 m^3/s in the sweep side and air at constant volume flow rate of 3.3E−7 m^3/s in the feed side, at 920 °C. They achieved constant oxygen permeation flux of 0.0126 mol/m^2-s over the 100 h period. They also obtained O_2 flux of 0.0091 mol/m^2-s when they replaced the inert helium gas with 1.083E−8 m^3/s of gaseous methane as fuel to enable oxy-methane combustion. They reported complete combustion of methane with excess O_2 flow rate of 20 ml/min. These two experimental conditions were modeled using the current model and the results obtained were reasonably compared within an error of less than 6% as shown in Fig. 4.

4.3. Oxygen permeation flux

The two-pass OTR geometry shown in Fig. 1 was optimized to support the combustion of methane with enough oxygen from the OTM for application in fire tube boilers. The geometric parameters that were optimized include: length of the OTM, surface area of the OTM, volume of the combustion annulus, thickness of inner-pipe and outer-pipe surface area. The lengths of the OTM studied ranges from 100 mm to 2000 mm. It was found that the oxygen permeation was insignificant after 500 mm. Hence the length of 5 mm of the OTM was considered. The outer surface area of the OTM was determined by the diameter at the fixed length. To obtain enough oxygen for the combustion, the membrane surface area should be reasonably large. Hence the diameter of the membrane was optimized to 200 mm based on the laminar velocity requirement due to typical membrane physical strength limitations as well as the higher oxygen partial pressure requirement for effective permeation from feed side to the sweep side. The volume of the combustion zone was determine based on the fuel flow rates as well as adequate residence time within the length of the OTM. It was found that a cross-sectional area if about 600 mm^2 was adequate for the 500 mm long OTM. This corresponds to the inner-pipe internal diameter of 34 mm. The thickness of the inner-pipe was also optimized to provide adequate heat transfer resistance to protect the low temperature combustion reaction from quenching. The thickness of 3 mm was adopted based on the thermal properties of the selected material. The outer-pipe surface area was determined based of the heat transfer rate requirements. This was related the velocity of the exit gases that transferred heat through convection as well as the outer-pipe temperature (load).

The oxygen permeation across the BSCF membrane was modeled by considering the fuel stream (CO_2) as sweep gas to convey the permeate

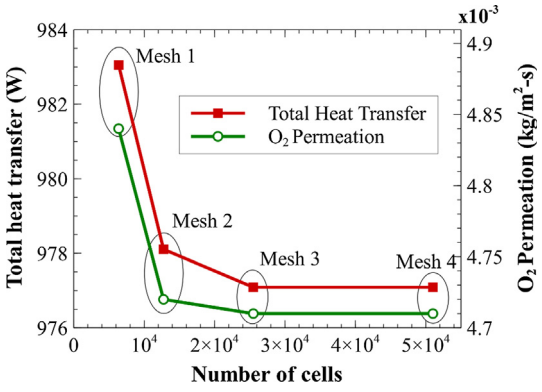

Fig. 2. Mesh independence analysis.

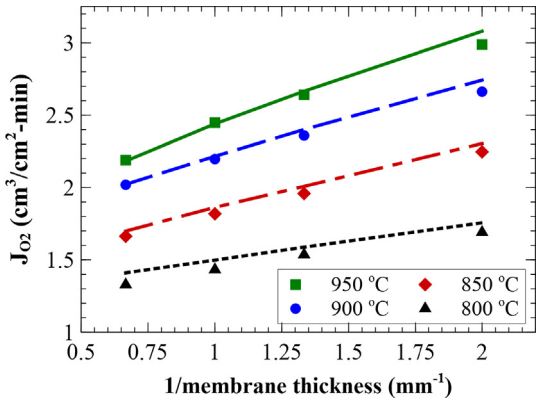

Fig. 3. Comparison of O_2 permeation flux between numerical and experimental data (solid lines from this numerical model and symbols from experimental work of Behrouzifar et al., [21]).

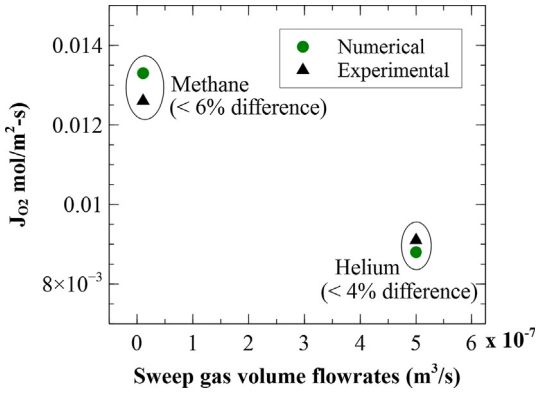

Fig. 4. Comparison of O_2 permeation flux between numerical and experimental data (circular symbols from this numerical model and triangular symbols from experimental work of Mezghani and Hamza [29].

and (CH_4 + CO_2) as sweep to react with the permeate. This was categorized into non-reactive and reactive conditions, respectively. In the non-reactive conditions, the fuel stream acted as a sweep gas only, in order to investigate the OTM permeation capabilities under several operating conditions. In the reactive conditions, the volumetric reaction model was used to simulate the species combustion reaction at the sweep zone. The oxygen permeation due to the two categories were presented in Figs. 5–8, under different conditions. The dependence of membrane temperature on the oxygen permeation flux has been fully established by many researchers where they fixed the membrane temperatures at elevated levels to improve permeation. But in practical applications, supplying the gases at elevated temperatures is more realistic. Hence, the inlet temperatures of the gases were varied to obtain an optimum temperature matrix for effective applications in both non-reactive and reactive conditions. Similarly, the effects of sweep and feed inlet mass flow rates as well as the diluent mass fractions were parametrized for the reactor optimization.

4.3.1. Effect of gases inlet temperature

The influence of feed and sweep inlet temperatures on the oxygen permeation flux across the OTM were shown in Fig. 5 for both the non-reactive and reactive conditions. As for the non-reactive conditions shown in Fig. 5-i, the effect of inlet temperature was considered for the fixed gases inlet mass flow rates of 5E − 4 kg/s based on an optimized near stoichiometric mixture condition. In Fig. 5-i(a), the sweep gas inlet temperature was fixed also at 900 °C, while the feed gas (air) temperatures were varied from 800 to 1000 °C. The oxygen permeation along the length of the membrane varied exponentially at all the feed inlet temperature conditions. The maximum permeations were observed at the sweep inlet due to the maximum oxygen partial pressure difference since there was no oxygen in the sweep stream, resulting the maximum driving force that led to maximum oxygen permeations. The oxygen permeation drops drastically near the inlets, along the membrane due to the increase in oxygen partial pressure at the sweep side which decreases the driving force. The oxygen partial pressure differences became nearly constant toward the trailing edge of the membrane. The higher the feed inlet temperature the higher the oxygen permeation flux, despite the little variations. This was attributed to the increase in partial pressure difference of oxygen at elevated temperatures. This trend was observed when the feed inlet temperature was fixed at 900 °C while varying the sweep inlet temperatures as shown in Fig. 5-i(b). The effect of the sweep inlet temperature resulted in slightly lower permeation in comparison to the feed effect. Even when both the feed and sweep gases inlet temperatures were varied sequentially (kept at the same value in each case), the oxygen permeation flux profiles along the OTM were similar. But the variations in permeation due to effect of temperature changes were more prominent.

The effect of inlet gases temperature on the oxygen permeation flux across the OTM for the reactive conditions are presented in Fig. 5-ii. The oxygen permeation trend near the sweep inlet started with the maximum value due to the maximum oxygen partial pressure difference between the feed and sweep sides and decreases sharply within the first 10 mm along the length of the OTM at all the inlet gas temperature conditions for the reactive cases. The oxygen permeation flux then suddenly shoots up after 10 mm to another maximum value as the result of the initiation of the combustion reaction which caused high temperature release. The temperature elevation due to oxy-methane reaction reduces the membrane surface exchange resistance thereby increasing the oxygen permeation. The increase in temperature has been reported to be responsible for higher oxygen vacancies disorder [44–46]. The surge in the oxygen permeation was also attributed to the oxygen consumption during the reaction near the membrane surface in the permeate side thereby reducing the partial pressure of the oxygen which consequentially increases the oxygen permeation driving force across the OTM. These phenomena were observed when the inlet gas temperature was more than 850 °C for the feed, sweep and both, as shown in Fig. 5-ii (a), (b) and (c), respectively. When the inlet gases were supplied at temperature range of 800 to 850 °C, the combustion reaction was quenched due to the low temperature within the combustion zone caused by the low temperature at the outer pipe. Hence the permeation profiles at lower temperature were similar to those discussed in the non-reactive conditions.

When the total oxygen permeation flux where computed for both the non-reactive and reactive conditions, as shown in Fig. 6, the effect of gases inlet temperature were more distinct. The higher the gases inlet temperature the more the oxygen permeation rate for all the inlet conditions. As for the non-reactive case, at lower gas inlet temperatures (below 900 °C), there was slight increase in oxygen permeation rate for the case of feed inlet conditions compared to the sweep due to the higher constant temperature of the sweep side (900 °C) for the feed case which led to the increase in oxygen vacancies disorder. While at higher gas inlet temperatures (above 900 °C) the reverse was the case, the feed temperature effect became lower than that of the sweep due to the same oxygen vacancies disorder. When both the feed and sweep gases inlet temperatures were the same, there was lower oxygen permeation at temperatures below 900 °C and higher permeation above 900 °C due to the double effect. The same trends were observed as for the case of reactive conditions with the feed case providing higher oxygen permeation at lower temperatures and slightly lower permeations at higher temperatures. As shown earlier in Fig. 5-ii, there was no combustion reaction influence at lower temperatures (below 900 °C) due to the low temperature effect.

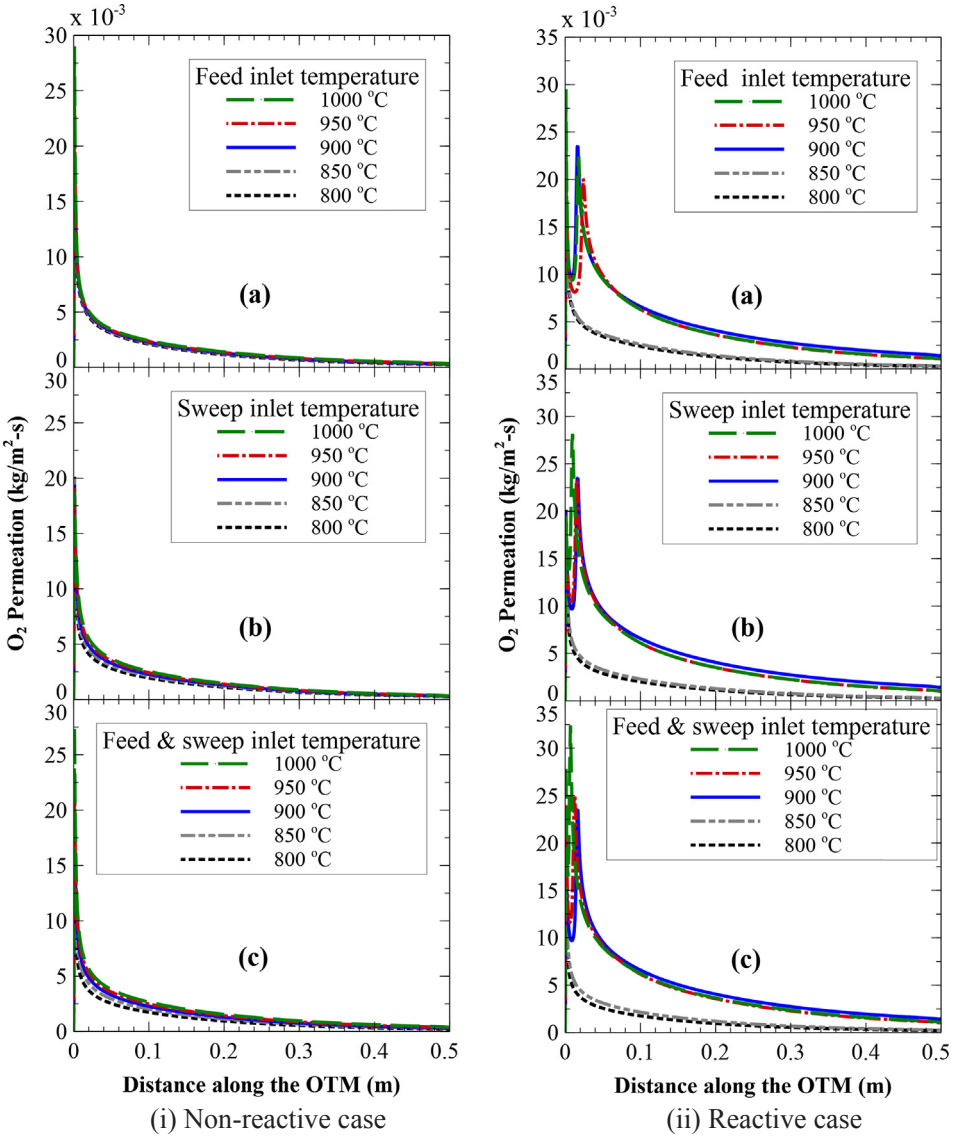

Fig. 5. Effect of gas inlet temperature on the rate of O_2 permeation flux across the OTM at an inlet gases flow rate of 5E-4 kg/s.

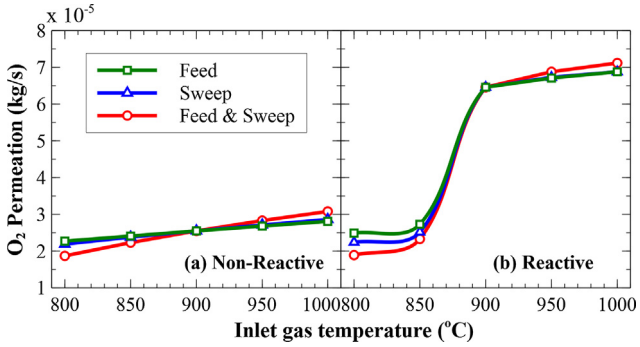

Fig. 6. Effect of gases inlet temperature on the rate of O_2 permeation across the OTM at inlet gases flow rate of 5E-4 kg/s.

4.3.2. *Effect of gases inlet mass flow rate*

The trend of the O_2 permeation flux profiles for the effect of gas inlet mass flow rate across the OTM at an inlet gases temperature of 900 °C were presented in Fig. 7 for both the non-reactive and reactive conditions. The mass flow rates were varied from 1E to 5 kg/s to 1E-3 kg/s in all cases. As for the non-reactive conditions as shown in Fig. 7-i, the higher the gases inlet mass flow rates the higher the oxygen permeation flux in all the cases. Increasing the feed inlet mass flow rates resulted in lower value of the maximum oxygen flux at the beginning of the OTM as compared to increase in sweep gas flow rates. This due to the increase in oxygen vacancies at the membrane surface in the sweep side as the result of higher sweep flow rates. The oxygen permeation flux drops drastically for all the non-reactive reactive condition along the length of the OTM due to the increase in oxygen concentration in the sweep zone which reduces the magnitude of the driving force by increasing the oxygen partial pressure at the sweep side.

As for the reactive conditions as shown in Fig. 7-ii, the effect of gas inlet mass flow rate on the oxygen permeation flux across the OTM were similar to the trends of the non-reactive cases at lower flow rates. When the feed gas inlet mass flow rate was considered the variable (Fig. 7-ii(a)), while the sweep gas was kept at a fixed flow rate of 5E − 4 kg/s and the inlet temperature of both inlet streams at 900 °C, there were increase in the oxygen permeation flux as the feed gas inlet mass flow rate increases at all the range of flow rates considered. The oxygen permeation at feed flow rates lower than 5E − 4 kg/s resulted in insufficient oxygen fluence to support steady combustion due to high sweep flow rate and thermal dilution effect of the 95% CO_2 in the 5E − 4 kg/s sweep flow rate. Hence, the combustion reaction was not

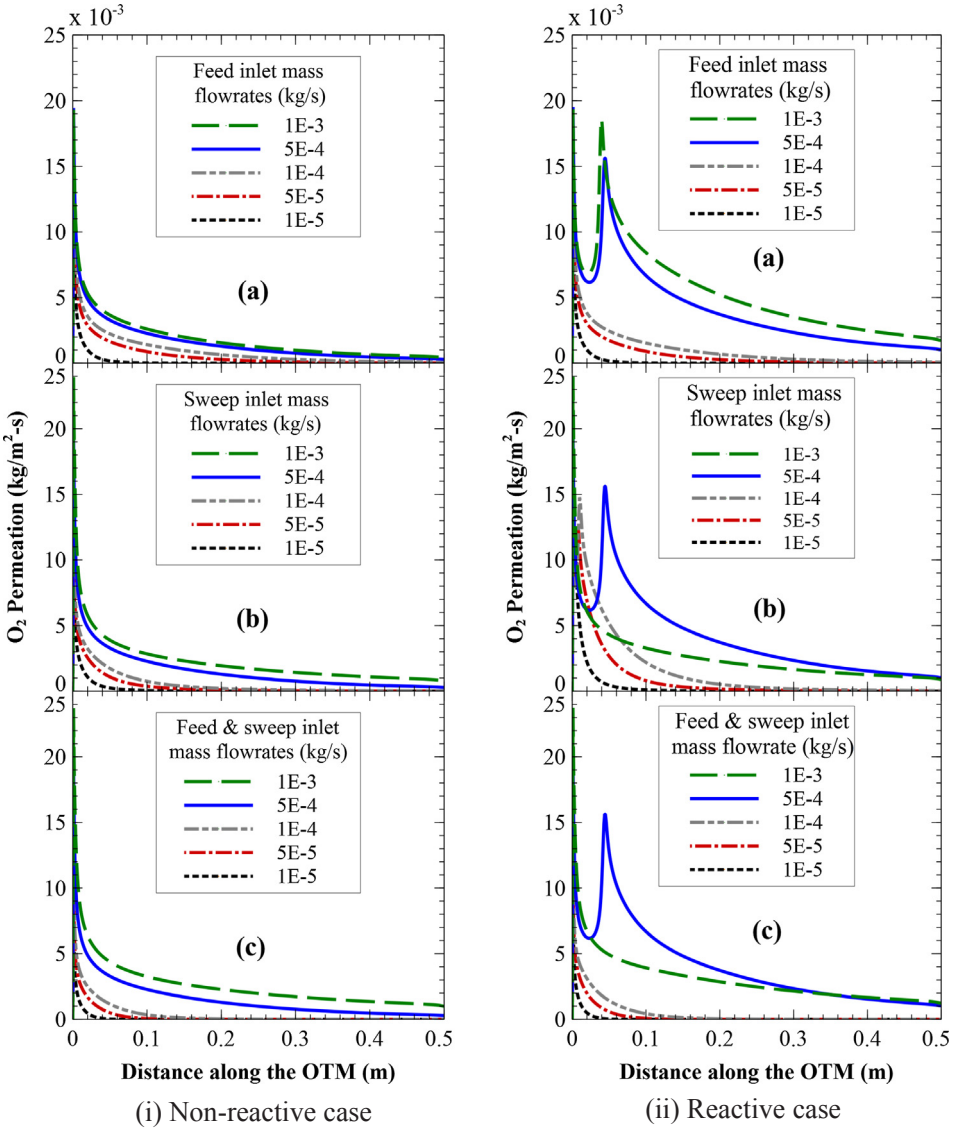

Fig. 7. Effect of gas inlet mass flow rate on the rate of O_2 permeation flux across the OTM at an inlet gases temperature of 900 °C.

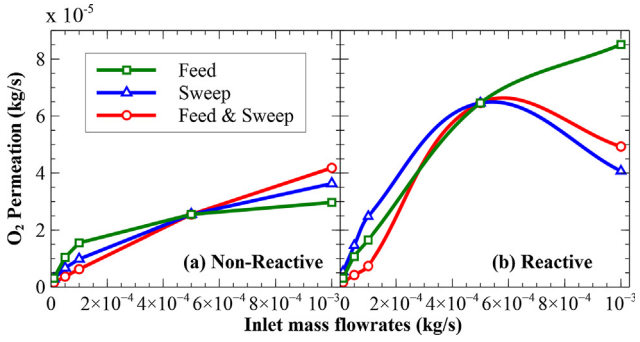

Fig. 8. Effect of gases inlet mass flow rate on the rate of O_2 permeation across the OTM at inlet gases temperature of 900 °C.

sustained, leading to the permeation profiles becoming similar to the non-reactive counter-parts. The combustion reaction was sustained when the feed gas inlet flow rates reached 5E − 4 kg/s with distinct oxygen permeation flux peak at the reaction zone as shown in Fig. 7-ii (a). This was attributed to the increase in oxygen consumption at the reaction zone which generated more oxygen vacancies on the permeate side of the membrane that consequently derived more oxygen across the OTM. The temperature raise due to oxy-methane reaction also decreases the membrane surface exchange resistance thereby increasing the oxygen permeation. When the sweep gas inlet mass flow rate was made the variable by fixing the feed gas inlet mass flow rate at 5E − 4 kg/s, the oxygen permeation trends were similar to the feed case as shown in Fig. 7-ii(b), but with highest combustion reaction intensity occurring at sweep gas inlet flow rate of 5E − 4 kg/s. When the sweep gas inlet mass flow rate exceeded 5E − 4 kg/s, its high velocity decreases the mixture residence time within the thermal protection zone (reaction zone) as well as further cooling the reaction zone due to the high content of the diluent thereby cooling the flame. This was also observed when both the feed and sweep inlet streams were kept at the same mass flow rates as shown in Fig. 7-ii(c), but with lowest permeation at lower inlet mass flow rates due to the double effect.

The effect of gases inlet mass flow rates on the total oxygen permeation flux for both the non-reactive and reactive conditions, were presented in Fig. 8, for the three inlet mass flow rate conditions. There was increase in the oxygen permeation rate due to increase in the inlet mass flow rate for all the inlet conditions when there was no reaction, as shown in Fig. 8-a. This was due to the simultaneous decrease in oxygen partial pressure at the sweep side. At higher gases inlet mass flow rate, beyond 5E − 4 kg/s, the effect of feed gas inlet temperatures

provided higher oxygen flow rates due to the sustained combustion reaction. The higher sweep inlet mass flow rates exceeding 5E − 4 kg/s resulted in lower oxygen permeation flux due to overwhelming sweep Reynolds number which lower the reaction zone temperature that quenched the flame. The oxygen permeation slightly increased when both the feed and sweep gases temperature were increased beyond 5E − 4 kg/s.

4.4. OTR heat transfer characteristics

4.4.1. Effect of gas inlet temperature on heat transfer

The oxy-methane combustion effects on the heat transfer to the outer-pipe (load) are presented in this section with focus on the effects of inlet gas temperature for constant feed and sweep inlet gases mass flow rate of 5E − 4 kg/s. These include both the convection and radiation components to evaluate the total heat transfer to the load. Fig. 9-i shows the effect of gas inlet temperatures on heat transfer to the load at fixed inlet gases mass flow rate of 5E − 4 kg/s for (a) feed, (b) sweep and (c) combined feed and sweep. The dash-dot line represents the convection component of the heat transferred to the load, the dash line represents the radiation component while the solid line is the total heat transferred to the load. As for Fig. 9-i(a), the sweep gas inlet temperature was kept constant at 900 °C while the feed gas inlet temperatures were varied from 800 to 1000 °C. The convection, radiation and the total heat transfers were found to increase with increase in the feed gas inlet temperature. At lower feed inlet temperatures (800–850 °C) the convective heat transfer rates was less than 180 W, which swiftly increase to about 310 W at 900 °C. This heat transfer surge was as the result of the combustion reaction that was sustained at 900 °C below which there was no significant reactions. The same heat transfer behavior was observed for the case of radiation heat transfer but the increase in the heat transfer rate was more than that of the convection heat transfer due to the high radiative emissivity of both the outer surface of the inner-pipe and the inner surface of the outer-pipe. The total heat transferred to the load was also replicated the same trend since it is the summation of the two. Hence the radiative heat transfer accounted for about 67–69% of the total heat transferred to the load while convection component was about 31–33%.

When the feed gas inlet temperature was maintained at 900 °C while the sweep gas inlet temperature was parameterized from 800 to 1000 °C, the heat transfer profiles were shown in Fig. 9-i(b). The heat transfer profiles were similar to the case of variable feed gas inlet temperatures discussed earlier. In comparison to the feed gas inlet temperature conditions, the convective heat transfer values were higher at lower sweep gas inlet temperatures due to and lower heat transfer values at higher sweep temperatures in. Likewise, the radiation heat

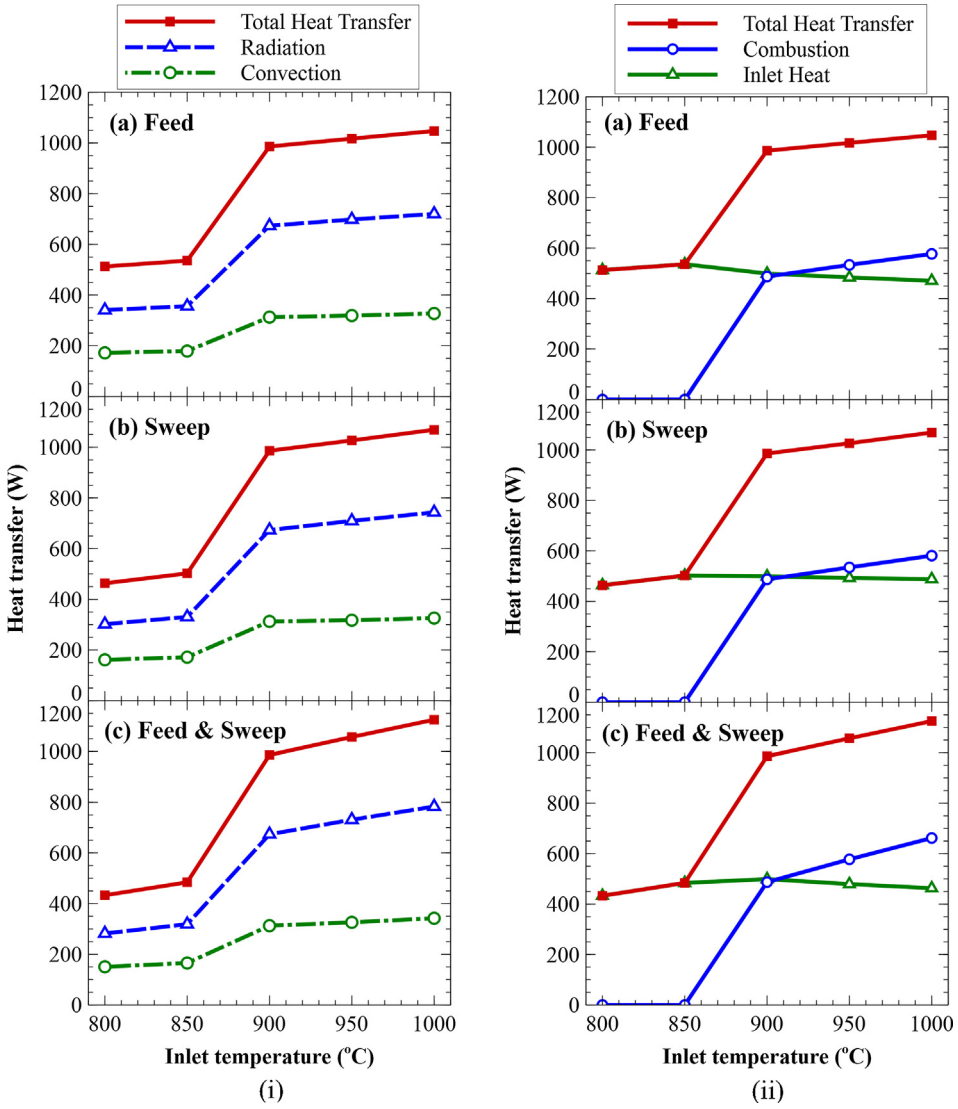

Fig. 9. Effect of gas inlet temperatures on heat transfer at inlet gases mass flow rate of 5E-4 kg/s: (i) Convection and Radiation, (ii) Combustion and Inlet heat.

transfer values were lower at lower sweep gas inlet temperatures and higher at higher sweep gas temperatures as compared to the feed counterparts. The lower heat transfer at lower sweep temperatures were attributed to the lower thermal energy content of the reaction zone mixture as compared with the feed case since there were no reaction. The higher heat transfer at higher sweep inlet gas temperatures was ascribed to the thermal energy release during the combustion reaction. The convective heat transfer at lower sweep inlet temperatures were slightly higher than that of the feed case due to the sweep gas temperature effect and lower at high sweep gas inlet temperatures due to the lower feed gas temperature. Nevertheless, the increase in the rate of heat transfer due to the gas inlet temperature effects were barely trivial (~1 W) for both non-reactive and reactive situations. The effect of maintaining the feed and sweep gases at the inlet temperatures as shown in Fig. 9-i(c), were almost the same as the effect sweep gas (Fig. 9-i(b)). This indicated that the heat transfer rates were merely dictated by the sweep gas inlet temperatures.

4.4.2. Effect of gas inlet temperature on combustion heat transfer

The contribution of the combustion heat released, and the gases initial inlet thermal heat were shown in Fig. 9-ii for the three gas inlet temperature conditions. These were evaluated based on the energy balance across the OTR boundaries. The heat transfers were assumed to be at steady state conditions thereby neglecting the heat required to preheat the inner-pipes. This enabled the assessment of combustion component of the overall heat transferred to the load. In all the three conditions examined in this part (Fig. 9-ii(a-c)), the combustion heat contribution at inlet gas temperatures below 900 °C was insignificant due to the flame quenching at steady state. Hence, all the heat transferred to the load were mainly via the inlet gases heat contents. This can be seen in Fig. 9-ii were the inlet gas component overlapped with the total heat transferred to the load while the combustion heat transferred was merely zero. There were roughly equal contributions between the combustion heat transferred and the gas inlet thermal heat transferred when all the gases were supplied at 900 °C. This was depicted by the coincidence of both the heat transfer components at the same values, as shown in Fig. 9-ii. When the gases inlet temperatures were beyond 900 °C, the combustion component of the heat transferred to the load increases with increase in gas temperatures due to the increase in the overall combustor energy level while the inlet contribution decreases at all the three conditions.

At feed inlet gas temperatures beyond 900 °C, while the sweep gas inlet temperature was kept constant at 900 °C (Fig. 9-ii(a)), the amount of combustion heat transferred to the load was lower than the heat transferred for the sweep gas cases (Fig. 9-ii(b)). This was due to the fact that increasing sweep gas inlet temperature led to more heat

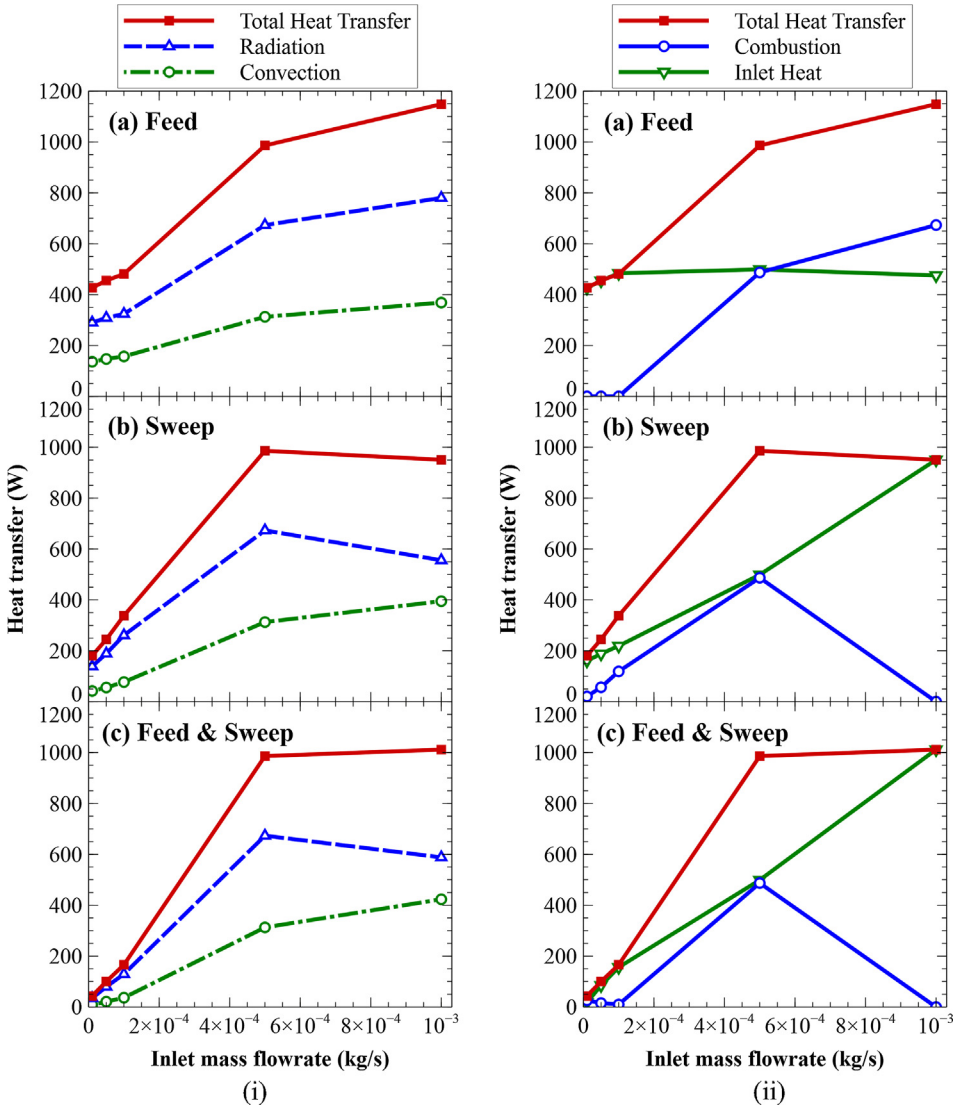

Fig. 10. Effect of gas inlet mass flow rates on heat transfer at inlet gases temperature of 900 °C: (i) Convection and Radiation, (ii) Combustion and Inlet heat.

transfer attributable to the increase in both convection and radiation. When both the feed and sweep gas inlet temperatures where varied, as shown in Fig. 9-ii(c), there were much higher increase in the amount of heat transferred to the load as compared to the individual streams, beyond 900 °C. This was correlated to the increase in both convection and radiation heat transferred as the result of higher energy level of the OTR. As for the gases inlet heat contributions, the sweep gas effect contributed the most as compared to the feed effect, this was due to direct contact of the sweep gas with the outer-pipe which aided the heat transfer.

4.4.3. Effect of gas inlet mass flow rate on heat transfer

Effect of gas inlet mass flow rates on heat transfer to the outer-pipe (load) at fixed inlet gases temperature of 900 °C while varying the mass flow rates from 1E to 5 to 1E-3 kg/s for (a) feed, (b) sweep and (c) feed and sweep conditions were studied in this section and the results were presented in Fig. 10-i. As for the condition whereby, the feed gas inlet mass flow rate was varied from 1E to 5 to 1E − 3 kg/s while keeping the sweep gas inlet mass flow rate constant at 5E − 4 kg/s indicated increase in both convection and radiation heat transferred to the load consequently increased the total heat transferred as the feed gas mass flow rate was increased, as shown in Fig. 10-i(a). This increase was meager at low feed flow rates (1E − 5 to 1E − 4 kg/s) due to lack of combustion reaction but surged afterwards as the result of the chemical energy released during combustion reaction. In a similar fashion with the effect of feed gas inlet temperatures, the radiation component of the total heat transferred was twice that of convection heat transferred at all the feed gas inlet flow rates. This is due to the radiative properties of the CO_2-rich exhaust gas mixture as well as the high emissivity of the inner radiating surfaces in contrast to the convective heat transfer coefficient of the same mixture. At feed gas inlet mass flow rate of 5E − 4 kg/s, the total heat transferred was about 1000 W out of which 68% was by radiation. This increased to about 1150 W at feed gas inlet flow rate of 1E − 3 kg/s.

The effect of sweep gas inlet mass flow rates on the heat transfer to the load at fixed feed gas inlet mass flow rate of 5E − 4 kg/s, were presented in Fig. 10-i(b). Under this condition, the rate of heat transfer at low sweep flow rates were less than that of the feed case with convection component being below 80 W, radiative component below 270 W and the total heat transferred was below 340 W, even at sweep gas inlet mass flow rate of 1E − 4 kg/s. This was due to the low thermal energy content of the sweep gas at low flow rates (< 5E − 4 kg/s) since there was no combustion reaction at these conditions. It was interesting to note that the maximum radiative and total heat transferred to the load occurred at sweep gas inlet mass flow rates of 5E − 4 kg/s, as shown in Fig. 10-i(b), beyond which the they decreased. Meanwhile the convection heat transferred continued to increase with increase in the sweep gas inlet mass flow rates. The decrease in the radiative heat transfer when the sweep gas inlet mass flow rate exceeded 5E − 4 kg/s, was attributed to the low reactivity of the mixture due to low residence time within the thermal protection zone (reaction zone) as well as further cooling the reaction zone due to the high content of the diluent. This phenomenon was also observed when both the feed and sweep inlet streams were kept at the same mass flow rates as shown in Fig. 10-i (c), but with slight improvement in the radiative heat transferred at higher sweep gas flow rate due to the feed effect. This indicated that the sweep gas inlet mass flow rate is among the most decisive controlling parameters in the total heat transfer to the load.

4.4.4. Effect of gas inlet mass flow rate on combustion heat transfer

Fig. 10-ii shows the effect of gas inlet mass flow rates on combustion heat transfer and the gases inlet thermal heat transferred to the load at constant inlet gases temperature of 900 °C while varying the mass flow rates from 1E to 5 to 1E − 3 kg/s for (a) feed, (b) sweep and (c) feed and sweep conditions. As we have seen in the previous discussions, the contributions of the chemical heat released during combustion was negligible at low flow rate feed gas inlet mass flow rates between 1E and 5 to 1E − 4 kg/s as shown in Fig. 10-ii(a). The inlet thermal heat contributed to all the heat transferred (426 to 455 W) to the load. Although there was slight increase in the inlet gas thermal heat transferred of about 30 W when the feed gas inlet mass flow rate was increased to 5E − 4 kg/s, the combustion reaction contributed almost equivalent rate of heat transfer at steady state. Hence the total heat transfer was elevated to about 1000 W, as the result of the double effect. There was increase in the combustion heat transfer due to increase in the feed gas inlet mass flow rate beyond 5E − 4 kg/s due to the increase in the oxygen permeation resulting in increased oxy-fuel reaction which raised the OTR overall thermal energy. The inlet gas thermal heat contribution slightly decreased but remained relatively constant despite the increase in the feed gas flow rate.

Fig. 10-ii(b) depicted the effect of sweep gas inlet mass flow rate variations at fixed feed gas inlet mass flow rate of 5E − 4 kg/s on the combustion heat transfer to the load. From the results, there were limited combustion reactions at low sweep gas inlet mass flow rates as indicated by low combustion heat transfer contributions which increases with increase in the sweep gas flow rate to the maximum at 5E − 4 kg/s. It was affirmed that there was no combustion reaction at sweep gas inlet mass flow rate of 1E − 3 kg/s due to zero combustion contribution. The gases inlet heat transferred to the load was proportional to the increase in the sweep gas flow rate due to the increase in the rate specific energy of the sweep gas. There was almost no combustion reaction when both the feed and sweep gases flow rates were fixed between 1E and 5 to 1E-4 kg/s due to insufficient oxygen permeation flux to sustain steady reaction, as shown in Fig. 10-ii(c). The only mass flow rate condition that sustained steady combustion was when both the gas streams were at 5E − 4 kg/s. The combustion reaction was extinguished at 1E − 3 kg/s of both the streams due to the flow speed overwhelming the laminar flame speed.

4.5. Number OTR units for fire-tube boiler application

The results of the total heat transfer to the load at base condition of the current design, a single unit of the OTR supplies about 1000 W (1 kW), with combustion heat transfer contributing 50% of the total heat. To supply 1–5 MWe, there should be 1000–5000 units of the OTRs based on the total heat supply. By considering only the combustion component, there should be 2000–10,000 units of the OTRs. The current design of the OTR has an outer diameter of 0.05 m and a nominal longitudinal distance of 0.505 m. Hence, the total surface area of the 1 mm membrane required will be 63.5–317 m^2 to deliver the required power output based on first law thermodynamic efficiency.

5. Conclusion

The numerical modeling of the two-pass oxygen transport membrane reactor for oxygen permeation and oxy-fuel combustion characteristics analyses for fire tube boilers application revealed that, for the non-reactive conditions, the effects of increase in gases inlet temperature in the range of 800–1000 °C, and mass flow rates in the range of 1E − 5–1E − 3 kg/s, on oxygen permeation along the length of the membrane was meager within the scope of this study. The higher the gases inlet conditions studied the higher the oxygen permeation flux in all the cases. The gases inlet temperature and mass flowrate dictate the rate of oxygen permeation under reactive conditions. Also, the gases inlet temperature and mass flow rates control the amount of heat transfer to the load. The sweep gas inlet condition was more critical to the stability of the combustion reaction. The current design of the proposed OTM reactor can deliver power output in the range from 1 to 5 MWe, based on 1 mm thick membrane with total surface area in the range of 63.5–317 m^2.

Acknowledgement

The authors would like to acknowledge the support of King Fahd University of Petroleum and Minerals (KFUPM) and SABIC to this work through project no. ME 2394.

References

[1] IEA. World Energy Outlook 2014; 2014. http://doi.org/10.1787/weo-2014-en.
[2] IEA. Technology Roadmap Carbon Capture and Sotrage in Industrial Applications; 2011. p. 43.
[3] Zhang Z, Borhani TNG, El-Naas MH. Carbon capture. Exergetic, Energy Environ Dimens 2018:997–1016. https://doi.org/10.1016/B978-0-12-813734-5.00056-1.
[4] Figueroa JD, Fout T, Plasynski S, McIlvried H, Srivastava RD. Advances in CO2 capture technology—the U.S. Department of Energy's carbon sequestration program. Int J Greenh Gas Control 2008;2:9–20. https://doi.org/10.1016/S1750-5836(07)00094-1.
[5] Yin C, Yan J. Oxy-fuel combustion of pulverized fuels: combustion fundamentals and modeling. Appl Energy 2016;162:742–62. https://doi.org/10.1016/j.apenergy.2015.10.149.
[6] Buhre BJP, Elliott LK, Sheng CD, Gupta RP, Wall TF. Oxy-fuel combustion technology for coal-fired power generation. Prog Energy Combust Sci 2005;31:283–307. https://doi.org/10.1016/j.pecs.2005.07.001.
[7] Ben-Mansour R, Habib MA, Nemitallah MA, Rajhi M, Suara KA. Characteristics of oxyfuel and air-fuel combustion in an Industrial Water Tube Boiler. Heat Transfer Eng 2014;35. https://doi.org/10.1080/01457632.2014.888920.
[8] Habib MA, Ahmed P, Ben-Mansour R, Mezghani K, Alam Z, Shao-Horn Y, et al. Experimental and numerical investigation of La_2 NiO_4 membranes for oxygen separation: geometry optimization and model validation. J Energy Resour Technol 2015;137:031102https://doi.org/10.1115/1.4029670.
[9] Hu Y, Yan J. Characterization of flue gas in oxy-coal combustion processes for CO2 capture. Appl Energy 2012;90:113–21. https://doi.org/10.1016/j.apenergy.2011.03.005.
[10] Hu Y, Yan J, Li H. Effects of flue gas recycle on oxy-coal power generation systems. Appl Energy 2012;97:255–63. https://doi.org/10.1016/j.apenergy.2011.12.096.
[11] Habib MA, Badr HM, Ahmed SF, Ben-Mansour R, Mezghani K, Imashuku S, et al. A review of recent developments in carbon capture utilizing oxy-fuel combustion in conventional and ion transport membrane systems. Int J Energy Res 2011;35:741–64. https://doi.org/10.1002/er.1798.
[12] Sunarso J, Hashim SS, Zhu N, Zhou W. Perovskite oxides applications in high temperature oxygen separation, solid oxide fuel cell and membrane reactor: a review. Prog Energy Combust Sci 2017;61:57–77. https://doi.org/10.1016/J.PECS.2017.03.003.
[13] Hong J, Kirchen P, Ghoniem AF. Numerical simulation of ion transport membrane reactors: oxygen permeation and transport and fuel conversion. J Membr Sci 2012;407–408:71–85. https://doi.org/10.1016/j.memsci.2012.03.018.
[14] Mancini ND, Mitsos A. Ion transport membrane reactors for oxy-combustion – Part I: Intermediate-fidelity modeling. Energy 2011;36:4701–20. https://doi.org/10.1016/j.energy.2011.05.023.
[15] Zhu X, Sun S, Cong Y, Yang W. Operation of perovskite membrane under vacuum and elevated pressures for high-purity oxygen production. J Membr Sci 2009;345:47–52. https://doi.org/10.1016/j.memsci.2009.08.020.
[16] Lu H, Cong Y, Yang WS. Oxygen permeability and stability of Ba 0.5 Sr 0.5 Co 0.8 Fe 0.2 O 3Àd as an oxygen-permeable membrane at high pressures n.d. doi: 10.1016/j.ssi.2005.10.030.
[17] Habib MA, Nemitallah MA. Design of an ion transport membrane reactor for application in fire tube boilers. Energy 2015;81:787–801. https://doi.org/10.1016/J.ENERGY.2015.01.029.
[18] Di Felice L, Middelkoop V, Anzoletti V, Snijkers F, van Sint Annaland M, Gallucci F. New high temperature sealing technique and permeability data for hollow fiber BSCF perovskite membranes. Chem Eng Process Process Intensifier 2016;107:206–19. https://doi.org/10.1016/j.cep.2014.12.004.
[19] Mezghani K, Hamza A, Habib MA, Lee D, Shao-Horn Y. Effect of microstructure and thickness on oxygen permeation of La2NiO4 + δ membranes. Ceram Int 2016;42:666–72. https://doi.org/10.1016/j.ceramint.2015.08.163.
[20] Ghadimi A, Alaee MA, Behrouzifar A, Asadi AA, Mohammadi T. Oxygen permeation of BaxSr1 − xCo0.8Fe0.2O3 − δ perovskite-type membrane: experimental and modeling. Desalination 2011;270:64–75. https://doi.org/10.1016/J.DESAL.2010.11.022.
[21] Behrouzifar A, Asadi AA, Mohammadi T, Pak A. Experimental investigation and mathematical modeling of oxygen permeation through dense Ba 0.5Sr 0.5Co 0.8Fe 0.2O 3-δ (BSCF) perovskite-type ceramic membranes. Ceram Int 2012;38:4797–811. https://doi.org/10.1016/j.ceramint.2012.02.068.
[22] Hong WK, Choi GM. Oxygen permeation of BSCF membrane with varying thickness and surface coating. J Membr Sci 2010;346:353–60. https://doi.org/10.1016/j.memsci.2009.09.056.
[23] Sunarso J, Liu S, Lin YS, Diniz da Costa JC. Oxygen permeation performance of BaBiO3-δ ceramic membranes. J Membr Sci 2009;344:281–7. https://doi.org/10.1016/j.memsci.2009.08.019.
[24] Ahmed P, Habib MA, Ben-Mansour R, Jamal A. Investigation of oxygen permeation through disc-shaped BSCF ion transport membrane under reactive conditions. Int J Energy Res 2017;41:1049–62. https://doi.org/10.1002/er.3696.
[25] Ben-Mansour R, Adebiyi AA, Habib MA. Investigation of performance of fire-tube boilers integrated with ion transport membrane for oxy-fuel combustion. Int J Energy Res 2016;40:1673–87. https://doi.org/10.1002/er.3553.
[26] Nemitallah MA, Habib MA, Salaudeen SA, Mansir I. Hydrogen production, oxygen separation and syngas oxy-combustion inside a water splitting membrane reactor. Renew Energy 2017;113:221–34. https://doi.org/10.1016/j.renene.2017.05.086.
[27] Khalil AEE, Gupta AK. Flame fluctuations in Oxy-CO2-methane mixtures in swirl assisted distributed combustion. Appl Energy 2017;204:303–17. https://doi.org/10.1016/j.apenergy.2017.07.037.
[28] Castillo R. Thermodynamic analysis of a hard coal oxyfuel power plant with high temperature three-end membrane for air separation. Appl Energy 2011;88:1480–93. https://doi.org/10.1016/j.apenergy.2010.10.044.
[29] Mezghani K, Hamza A. Application of Ba0.5Sr0.5Co0.8Fe0.2O3 − δ membranes in an oxy-fuel combustion reactor. J Membr Sci 2016;518:254–62. https://doi.org/10.1016/J.MEMSCI.2016.07.001.
[30] Nemitallah MA. A study of methane oxy-combustion characteristics inside a modified design button-cell membrane reactor utilizing a modified oxygen permeation model for reacting flows. J Nat Gas Sci Eng 2016;28:61–73. https://doi.org/10.1016/j.jngse.2015.11.041.
[31] Hong J, Kirchen P, Ghoniem AF. Laminar oxy-fuel diffusion flame supported by an oxygen-permeable-ion-transport membrane. Combust Flame 2013;160:704–17. https://doi.org/10.1016/J.COMBUSTFLAME.2012.11.014.
[32] Nemitallah M, Habib MA, Ben-Mansour R. Investigations of an ion transport membrane reactor specially designed for a power cycle. Appl Mech Mater 2013;302:440–6. https://doi.org/10.4028/www.scientific.net/AMM.302.440.
[33] Hu Y, Li H, Yan J. Numerical investigation of heat transfer characteristics in utility boilers of oxy-coal combustion. Appl Energy 2014;130:543–51. https://doi.org/10.1016/j.apenergy.2014.03.038.
[34] Kee RJ, Coltrin ME, Glarborg P. Chemically reacting flow: theory and practice. Wiley-Interscience; 2003.
[35] McGee HA. Molecular engineering. McGraw-Hill; 1991.
[36] Yang X, Clements A, Szuhánszki J, Huang X, Farias Moguel O, Li J, et al. Prediction of the radiative heat transfer in small and large scale oxy-coal furnaces. Appl Energy 2018;211:523–37. https://doi.org/10.1016/j.apenergy.2017.11.070.
[37] Kez V, Liu F, Consalvi JL, Ströhle J, Epple B. A comprehensive evaluation of different radiation models in a gas turbine combustor under conditions of oxy-fuel combustion with dry recycle. J Quant Spectrosc Radiat Transfer 2016;172:121–33. https://doi.org/10.1016/J.JQSRT.2015.11.002.
[38] Porter R, Liu F, Pourkashanian M, Williams A, Smith D. Evaluation of solution methods for radiative heat transfer in gaseous oxy-fuel combustion environments. J Quant Spectrosc Radiat Transfer 2010;111:2084–94. https://doi.org/10.1016/j.jqsrt.2010.04.028.
[39] Fluent A. Fluent 12. Theory guide; 2017.
[40] Xu SJ, Thomson WJ. Oxygen permeation rates through ion-conducting perovskite membranes. Chem Eng Sci 1999;54:3839–50. https://doi.org/10.1016/S0009-2509(99)00015-9.
[41] Yin C. Advanced modeling of oxy-fuel combustion of natural-gas. Tech. Rep. Department of Energy Technology, University of Aalborg; 2011.
[42] Andersen J, Rasmussen CL, Giselsson T, Glarborg P. Global combustion mechanisms for use in CFD modeling under oxy-fuel conditions. Energy Fuels 2009;23:1379–89. https://doi.org/10.1021/ef8003619.
[43] Ben-Mansour R, Ahmed Pervez, Habib MA, Jamal Aqil. Oxy-combustion of liquid fuel in an ion transport membrane reactor. Int J Energy Environ Eng 2018. https://doi.org/10.1007/s40095-017-0246-4.
[44] Chen X, Huang L, Wei Y, Wang H. Tantalum stabilized SrCoO3 − δ perovskite membrane for oxygen separation. J Membr Sci 2011;368:159–64. https://doi.org/10.1016/J.MEMSCI.2010.11.040.
[45] Yi J, Brendt J, Schroeder M, Martin M. Oxygen permeation and oxidation states of transition metals in (Fe, Nb)-doped BaCoO3 − δ perovskites. J Membr Sci 2012;387–388:17–23. https://doi.org/10.1016/J.MEMSCI.2011.08.053.
[46] Kruidhof H, Bouwmeester HJM, Doorn RHE, Burggraaf AJ. Influence of order-disorder transitions on oxygen permeability through selected nonstoichiometric perovskite-type oxides. Solid State Ionics 1993;63–65:816–22. https://doi.org/10.1016/0167-2738(93)90202-E.